

Machine learning generative models for automatic design of multi-material 3D printed composite solids

Tianju Xue^{a,*}, Thomas J. Wallin^b, Yigit Menguc^b, Sigrid Adriaenssens^a,
Maurizio Chiaramonte^{b,*}

^a Department of Civil and Environmental Engineering, Princeton University, Princeton, NJ 08544, USA

^b Facebook Reality Labs, Redmond, WA, 98052, USA

ARTICLE INFO

Article history:

Received 31 July 2020

Received in revised form 15 September 2020

Accepted 15 September 2020

Available online 23 September 2020

Keywords:

Mechanical metamaterial

Machine learning

3D printing

ABSTRACT

Mechanical metamaterials are artificial structures that exhibit unusual mechanical properties at the macroscopic level due to architected geometric design at the microscopic level. With rapid advancement of multi-material 3D printing techniques, it is possible to design mechanical metamaterials by varying spatial distributions of different base materials within a representative volume element (RVE), which is then periodically arranged into a lattice structure. The design problem is challenging, however, considering the wide design space of potentially infinitely many configurations of multi-material RVEs. We propose an optimization framework that automates the design flow. We adopt variational autoencoder (VAE), a machine learning generative model to learn a latent, reduced representation of a given RVE configuration. The reduced design space allows to perform Bayesian optimization (BayesOpt), a sequential optimization strategy, for the multi-material design problems. In this work, we select two base materials with distinct elastic moduli and use the proposed optimization scheme to design a composite solid that achieves a prescribed set of macroscopic elastic moduli. We fabricated optimal samples with multi-material 3D printing and performed experimental validation, showing that the optimization framework is reliable.

© 2020 Elsevier Ltd. All rights reserved.

1. Introduction

Mechanical metamaterials are artificial structures defined by their geometry rather than their chemical composition. Architected with multi-level structures, mechanical metamaterials exhibit unique macroscopic properties such as being ultralight and ultrastiff [1], pentamodal [2], auxetic [3], etc. The rapid growth of this field has been partly fueled by the advancement of manufacturing technologies such as additive manufacturing [4,5], which enables fast prototyping and economic small-scale production of materials with specific microstructures [6]. Among them, the emerging technique of multi-material 3D printing [7] reveals a promising direction of designing novel composite solids by combining multiple base materials with distinct properties [8,9].

We focus on elastic moduli control, an important subject in designing mechanical metamaterials [10]. The goal is to design a representative volume element (RVE) composed of different base materials so that when the RVEs are periodically arranged into a lattice structure, the macroscopic elastic moduli achieve

a desired set of values. Central to the design problems is the appropriate *parametric representation* of RVE structures. Standard topology optimization methods suffer from being computationally expensive due to voxel level parametrization [11]. To avoid direct parametrization of voxels, [12] pre-defines a set of manually constructed microstructure families and base the design on these templates. Still, traditional approaches like this need to go through trial-and-error design loops which involve domain expertise and intensive labor. Establishing an optimization framework where design parameters are selected automatically without human interference remains challenging. Those parameters must live in a relatively low dimensional space feasible for optimization while not losing their representation power. Our proposed optimization framework addresses the challenge using machine learning techniques.

Over the past few years, groundbreaking advances in machine learning provide new insight into the development of robust design strategies, particularly in mechanics, materials and structures [13–15]. New paradigms have emerged where complicated data structures are compressed into an effective lower dimensional space and designs are instead performed over such reduced space. This usually requires coupling of a generative model that maps from the reduced space to the original data space and a gradient-free optimization algorithm that operates over the

* Corresponding authors.

E-mail addresses: txue@princeton.edu (T. Xue), mchiaram@fb.com (M. Chiaramonte).

reduced space. Variational autoencoders (VAEs) [16] and generative adversarial networks (GANs) [17] are the two most popular generative models. Bayesian optimization (BayesOpt) [18], a sequential design strategy to seek global optimum, is usually adopted to couple with the generative models for optimization. Representative works using this coherent design strategy include but not limited to discovery of new molecules with desired properties [19], shape optimization for minimal drag force in fluid dynamics [20], finding optimal optical performance of composite materials [21], improvement in solution efficiency for heat conduction [22], etc.

In this work we propose an optimization framework that automates the procedures of designing composite mechanical metamaterials. We adopt VAEs to compress RVE images that describe the spatial distribution of base materials to a reduced latent space. As generative models, VAEs also provide a venue to recover RVE images from the latent space. We then use BayesOpt to find an optimal RVE configuration that fulfills the prescribed design goal. Within each iteration of BayesOpt, we need to compute the macroscopic elastic moduli. We take a systematic approach known as homogenization, a well established technique [23–26], for the evaluation of the effective macroscopic elastic moduli. After the optimization loop, we use multi-material 3D printing to fabricate samples and experimentally measure their elastic moduli for validation. Quantitative comparisons show that our scheme is applicable and reliable.

2. Computational homogenization for linear elasticity

Before proceeding to the design problem, we introduce the computational homogenization scheme, a key step in each iteration of BayesOpt. We consider a linear elasticity problem over a domain $\Omega \subset \mathbb{R}^2$. The problem (in the absence of body force) reads: Find the displacement field $\mathbf{u} : \Omega \rightarrow \mathbb{R}^2$ such that

$$\begin{aligned} \nabla \cdot \boldsymbol{\sigma} &= \mathbf{0} & \text{in } \Omega, \\ \mathbf{u} &= \mathbf{u}_b & \text{on } \partial\Omega^D, \\ \boldsymbol{\sigma} \cdot \mathbf{n} &= \mathbf{t} & \text{on } \partial\Omega^N, \end{aligned} \quad (1)$$

where $\boldsymbol{\sigma}$ is the stress tensor, \mathbf{u}_b is a known function defined on $\partial\Omega^D$, \mathbf{n} is the unit outward normal, \mathbf{t} is the traction applied on the boundary $\partial\Omega^N$, $\partial\Omega^N \cup \partial\Omega^D = \partial\Omega$ and $\partial\Omega^N \cap \partial\Omega^D = \emptyset$. The constitutive model can be defined by a strain energy density function

$$W = \frac{1}{2} \boldsymbol{\epsilon} : \mathbb{C} : \boldsymbol{\epsilon}, \quad (2)$$

where $\boldsymbol{\epsilon} = \frac{1}{2}(\nabla \mathbf{u} + \nabla \mathbf{u}^T)$ is the strain tensor and \mathbb{C} is the fourth order constitutive tensor.

The above formulation is based on a single, homogeneous material. Our composite solids are composed of multiple materials. The overall mechanical properties may significantly differ from each of the base material. Computational homogenization is a systematic approach to obtain “averaged” macroscopic mechanical properties. At the macroscopic level, we formulate the homogenized constitutive relationship as

$$\overline{W} = \frac{1}{2} \overline{\boldsymbol{\epsilon}} : \overline{\mathbb{C}} : \overline{\boldsymbol{\epsilon}}, \quad (3)$$

where $\overline{}$ denotes a macroscopic quantity. Given \mathbb{C} for each base material and RVE configuration of how they form the composite solid, our goal is to compute the macroscopic constitutive tensor $\overline{\mathbb{C}}$. We follow the treatment by [27], where the principle for homogenization is that the total strain energy stored in the RVE computed via Eqs. (2) and (3) must be equal for arbitrarily imposed macroscopic strain conditions. For further

details about computational homogenization of linear elasticity, see Appendix A.

In this work, the composite solids are made from two base materials: a commercial hard polyurethane (RPU) with measured Young's modulus $E_h = 1300$ MPa and Poisson's ratio $\nu_h = 0.23$ and a custom soft silicone (SilDN) [28] with $E_s = 0.12$ MPa and $\nu_s = 0.33$. We make plane stress assumption throughout the work. We further restrict the composite solids to preserving cubic symmetry as shown in Fig. 1. It can be shown that under these assumptions the constitutive tensor $\overline{\mathbb{C}}$ are fully described by three independent elastic moduli [29,30]. For example, it is common to pick Young's modulus \overline{E} , shear modulus \overline{G} and Poisson's ratio $\overline{\nu}$ as a complete set of description, in which case the macroscopic stress-strain relationship simplifies to

$$\begin{bmatrix} \overline{\sigma}_{11} \\ \overline{\sigma}_{22} \\ \overline{\sigma}_{12} \end{bmatrix} = \begin{bmatrix} \frac{\overline{E}}{1-\overline{\nu}^2} & \frac{\overline{\nu}\overline{E}}{1-\overline{\nu}^2} & 0 \\ \frac{\overline{\nu}\overline{E}}{1-\overline{\nu}^2} & \frac{\overline{E}}{1-\overline{\nu}^2} & 0 \\ 0 & 0 & \overline{G} \end{bmatrix} \begin{bmatrix} \overline{\epsilon}_{11} \\ \overline{\epsilon}_{22} \\ 2\overline{\epsilon}_{12} \end{bmatrix}. \quad (4)$$

As shown in Fig. 1, we summarize the computational homogenization problem as to find out the macroscopic elastic moduli $\{\overline{E}, \overline{\nu}, \overline{G}\}$ given an image-like description (binary pixel values indicating base material information) of a RVE. The computational homogenization technique requires the use of the Finite Element Method (FEM). We choose the open source FEM software FEniCS [31] for the implementation.

3. Composite mechanical metamaterials for elasticity control

One can view computational homogenization as a “forward problem” in that a description of RVE is given and the aim is to find the macroscopic elastic moduli $\{\overline{E}, \overline{\nu}, \overline{G}\}$. On the contrary, the design problem seeks an optimal RVE in order to achieve a prescribed set of macroscopic elastic moduli, so it is helpful to think about the design problem as an “inverse problem”. In our problem, the design space is the set of binary images, immediately leading to an intractable, high dimensional combinatorial optimization problem. We tackle the challenge by learning a reduced representation of the image data, and performing optimization over this low dimensional space instead. Once we obtain the optimal design, we use 3D printing to fabricate the corresponding composite solids and measure the macroscopic mechanical properties experimentally for validation.

3.1. Bayesian optimization over reduced space

The overall design flow is presented in Fig. 2. We prepare an artificial image database and train the VAE to generate realistic images. BayesOpt operates over the reduced latent space learned by the VAE and couples with the homogenization procedure introduced in Section 2.

VAEs are among the family of latent-variable models [32]. The observable RVE image data can be considered as samples drawn from a probability distribution $p(\mathbf{x})$ where $\mathbf{x} \in \mathcal{X}$ lives in a high dimensional space. Under the assumption, the high dimensional image data can be compressed into a low dimensional space without severe loss of information. We denote the associated low dimensional distribution as $p(\mathbf{z})$ where $\mathbf{z} \in \mathcal{Z}$ is the latent variable. VAEs provide a principled approach for learning latent-variable models by jointly training over two parametrized neural network models: the encoder or recognition model, and the decoder or generative model. VAEs generalize autoencoders and encourage the latent space to be continuous in producing valid decoded images, which qualifies as the design space for optimization.

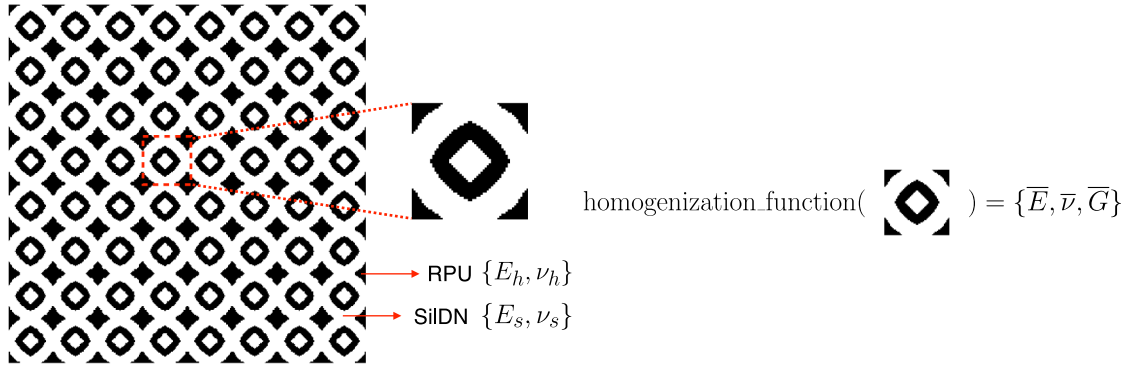


Fig. 1. Computational homogenization setup. Leftmost is a composite solid composed of two base materials RPU and SiIDN, with elastic moduli $\{E_h, \nu_h\}$ and $\{E_s, \nu_s\}$ respectively. A magnified RVE is also shown for clarity. Rightmost is the homogenization function, treated as a black-box function that takes the input of an image representation of a RVE and yields the output of the set of homogenized macroscopic elastic moduli $\{\bar{E}, \bar{\nu}, \bar{G}\}$.

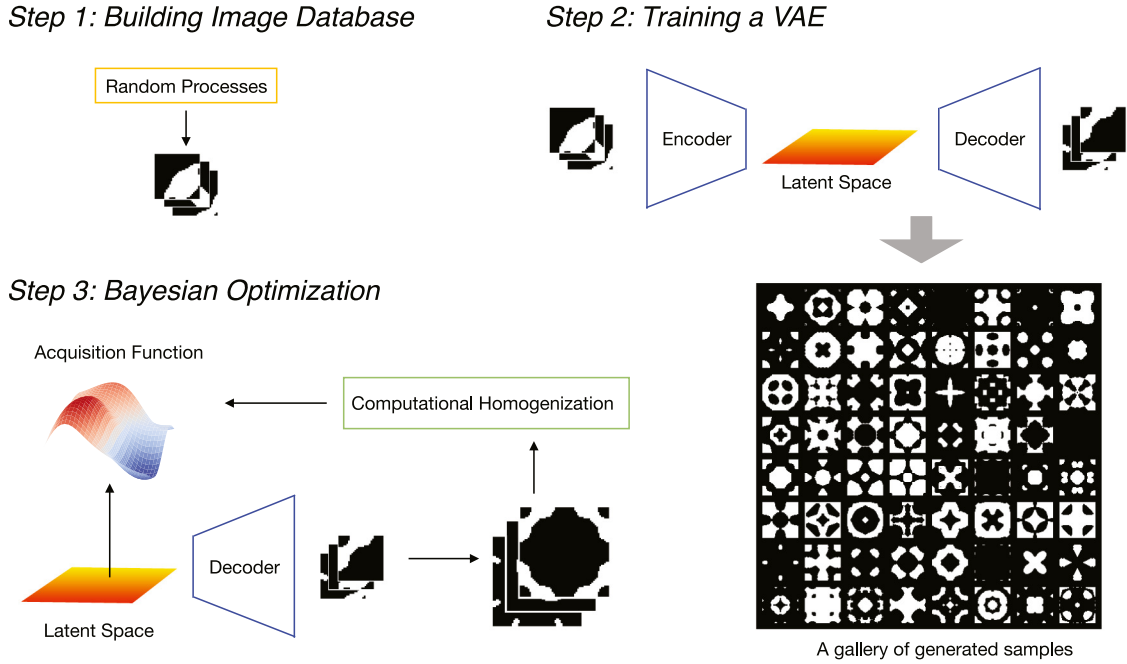


Fig. 2. The proposed optimization framework. Step 1: Draw samples from a random process to build the artificial database of RVE images (28×28 pixels for each image). Step 2: Train a VAE so that it generates realistic output samples. By flipping the 28×28 images twice we obtain the 56×56 RVE images that preserve symmetry. Step 3: BayesOpt towards optimal design of a RVE that achieves the prescribed macroscopic elastic moduli.

We implement the VAE model in PyTorch [33], an open source deep learning platform. The input to the VAE are images of size (*batch*, 1, 28, 28) while the output is of the same size. The input image database is constructed following a stochastic approach adopted in [34,35]. The method thresholds a Gaussian random field (GRF) to generate realistic binary representations of RVEs. The width for the hidden layer is set to be 10, namely, $\mathcal{Z} = \mathbb{R}^{10}$. The encoder part consists of two convolutional and two dense layers. Similarly, the decoder consists of two dense layers followed by two deconvolutional layers. Right before the output layer we add an additional constraint to force diagonal symmetry on the output tensors. To generate new samples, we only need the decoder model. We draw random variables from a unit Gaussian distribution as the input to the decoder and threshold the decoded images to reconstruct the binary composition. Fig. 2 shows a gallery of generated RVE samples. A more detailed description on VAEs can be found in Appendix B.

To further demonstrate the feasibility of optimizing over the latent space \mathcal{Z} , we draw 200 samples from $p(\mathbf{z})$, obtain decoded RVE images, and perform computational homogenization.

For visualization purpose, we use principal component analysis (PCA) [36] to compress the latent space into a 2-dimensional space and show the results in Fig. 3. As shown, the latent space demonstrates a continuous variation for the macroscopic Young's modulus \bar{E} and the macroscopic shear modulus \bar{G} , while a less clear trend is observed for macroscopic Poisson's ratio $\bar{\nu}$. This is not surprising, though, as adjusting \bar{E} or \bar{G} is straightforward by allocating RPU (hard material) and SiIDN (soft material) in different proportions to the RVE, yet to get a desired $\bar{\nu}$ is not immediately obvious from the perspective of a human expert. It is therefore expected that the optimization towards a tailored $\bar{\nu}$ be more difficult than \bar{E} or \bar{G} .

We next show that coupled with BayesOpt, we are able to design a RVE that simultaneously achieves desired \bar{E} and $\bar{\nu}$. Formally, we state our design problem as an optimization problem:

$$\mathbf{z}^* = \arg \max_{\mathbf{z} \in \mathcal{Z}} f(\mathbf{z}), \quad (5)$$

where $f(\mathbf{z}) = \text{cost_function}(\text{homogenization_function}(\text{decoder_function}(\mathbf{z})))$ is treated as a black-box function. The

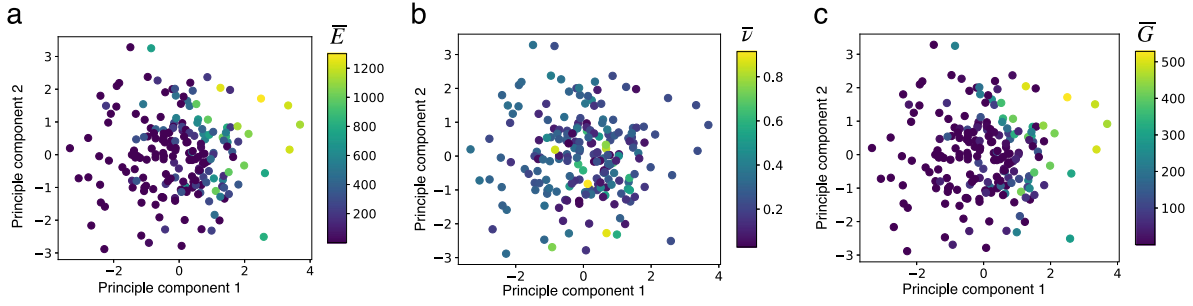


Fig. 3. PCA plots for latent space carrying information of the macroscopic elastic moduli.

decoder_function is the decoder part of the VAE model. The homogenization_function is discussed in Section 2. We define cost_function as

$$\text{cost_function}(\{\bar{E}, \bar{\nu}, \bar{G}\}) = e^{-(\bar{E} - \hat{E}_t)^2 - (\bar{\nu} - \hat{\nu}_t)^2}, \quad (6)$$

where

$$\begin{aligned} \hat{E} &= \frac{\log(\bar{E}) - \log(E_s)}{\log(E_h) - \log(E_s)}, & \hat{\nu} &= \frac{\bar{\nu} - \nu_h}{\nu_s - \nu_h}, \\ \hat{E}_t &= \frac{\log(\bar{E}_t) - \log(E_s)}{\log(E_h) - \log(E_s)}, & \hat{\nu}_t &= \frac{\bar{\nu}_t - \nu_h}{\nu_s - \nu_h}, \end{aligned} \quad (7)$$

with $\bar{E}_t = 260$ MPa and $\bar{\nu}_t = 0.4$ being set as the design goal. These numbers are arbitrarily selected and only serve for the purpose of a concrete demonstration of the proposed methodology. The cost_function considers normalized quantities (denoted by $\hat{\cdot}$) to alleviate the effect of various length scales of different quantities.

The computational cost to evaluate the objective function in Eq. (5) is not cheap, motivating the use of BayesOpt, a class of machine-learning-based optimization methods. BayesOpt builds a probabilistic surrogate model for the objective function and queries the next data point by minimizing an expected loss function. The optimization loop is completely automatic and avoids subjective human decisions in trial-and-error design. In this work, we use noise free Gaussian process regression as the surrogate model for BayesOpt. We apply expected improvement, a classic acquisition function to determine the next data point to sample. The searching process in principle tries to gain a balance between exploitation and exploration. We point to [37,38] for comprehensive descriptions of BayesOpt.

We adopt an open source library BoTorch [39] for BayesOpt. We evaluate the objective function values for 100 randomly generated RVEs for warm-up and obtain the objective value to be around 0.8, considered as a suitable initial point. Then, we start BayesOpt and plot the current best objective values with respect to the iteration number. We terminate the optimization when the current best objective value is close to 1, which is the theoretical limit when the elastic moduli of the optimized RVE perfectly match the targets. As shown in Fig. 4, the optimized RVE has the macroscopic elastic moduli:

$$\begin{aligned} \{\bar{E}^*, \bar{\nu}^*, \cdot\} \\ = \text{homogenization_function}(\text{decoder_function}(z^*)), \end{aligned} \quad (8)$$

which are close to the target values $\{\bar{E}_t, \bar{\nu}_t, \cdot\}$ measured in the normalized sense.

3.2. Experimental validation

We fabricate the three highlighted samples in Fig. 4 and measure their mechanical properties for experimental validation.

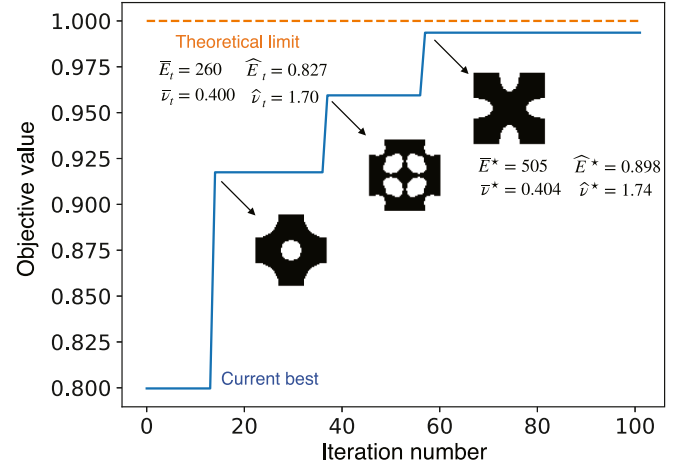


Fig. 4. Iterations of BayesOpt. The objective function is defined using Eq. (5). The theoretical limit is achieved only if the macroscopic elastic moduli exactly match the desired values. Three RVEs are plotted on the path to optimum. The third RVE is the optimal one with \bar{E}^* and $\bar{\nu}^*$ close to the targets \bar{E}_t and $\bar{\nu}_t$.

Both RPU and SiIDN photopolymerize from low viscosity precursors which enables high resolution Stereolithography (SLA, see Fig. 5) 3D printing of arbitrary structures like those generated by the VAE. Strong interfacial bonding between material layers remains a significant challenge to 3D printing multimaterial combined structures. Our chosen materials are “dual-stage” polymers; photo-crosslinking during 3D printing sets the object’s shape followed by a second, condensation based crosslinking reaction that improves the mechanical robustness. [40] recently employed this latent condensation reaction to cohesively bond 3D printed materials to substrates spanning seven orders of magnitude in Young’s Modulus. Though possible to SLA print directly using resin-exchange methods, manufacturing ease and rapid iteration led us to combine SLA printing and UV-assisted replica molding (see Fig. 5) when fabricating our multimaterial structures. Briefly, we first print (Carbon™ M2 printer) the RPU structure onto a release film and then cast the SiIDN precursor into the voids. Temporarily clamping a flat, transparent substrate coated with Teflon on top of the printed structure removes excess resin and the subsequent irradiation solidifies the SiIDN material. Interfacial crosslinks between RPU and SiIDN form during the second stage of curing at room temperature ($t \sim 15$ h) followed by thermal treatment at 120°C ($t \sim 8$ h).

With samples fabricated, we experimentally validated our design strategy via tensile tests. As shown in Fig. 6, our experimentally measured values for macroscopic elastic moduli generally agree with the computational homogenization predicted trends. The predicted Poisson’s ratios fall within the error of the measured values. However, the actual Young’s modulus values are

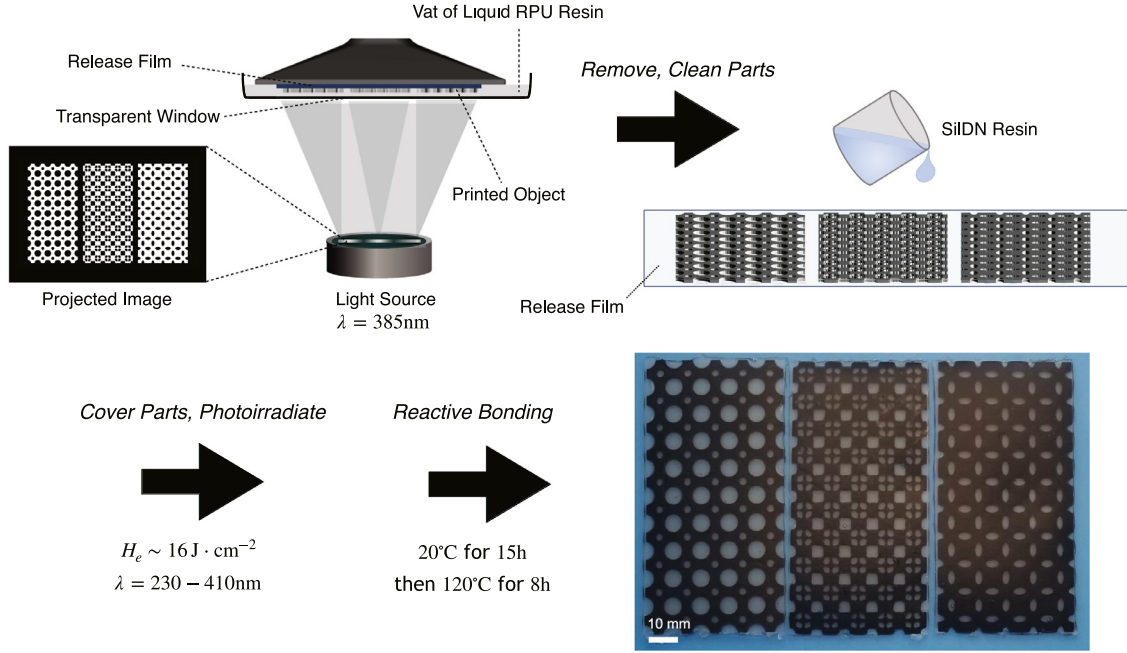


Fig. 5. Detailed procedures of multi-material 3D printing. We fabricate the three highlighted samples matching the ones presented in Fig. 4.

consistently higher than predictions. We postulate that the manufacturing process of the composite materials could have consistently favored RPU over SiIDN, leading to a higher macroscopic Young's modulus. Also, the samples (see Fig. 5) contain only a finite number RVEs and the measurement could have been affected by the boundary effects, whereas the computational homogenization essentially assumes infinite size of samples. It is important to note that while the composite solid yields an intermediate modulus ($E_s < \bar{E} < E_h$), this strategy can obtain Poisson's ratios beyond the range found between the base materials ($\nu_h < \nu_s < \bar{\nu}$). Thus confirming the ability to obtain novel material properties via mechanical design of metamaterials. For completeness, Table 1 gives a summary of the target values, optimization results, and experiment outcomes.

In Table 1, we notice that the optimization result of \bar{E}^* (505 MPa) is still much larger than the target value \bar{E}_t (260 MPa), while the optimization result of $\bar{\nu}^*$ (0.404) is relatively close to the specified $\bar{\nu}_t$ (0.4). However, the discrepancy is smaller under the normalized metric, with \bar{E}^* (0.898) close to \bar{E}_t (0.827) and $\bar{\nu}^*$ (1.74) close to $\bar{\nu}_t$ (1.70). The actual optimization is implemented using the normalized metric. There is no obvious evidence showing either optimizing towards a tailored Young's modulus or Poisson's ratio is easier, in contrast to our original speculation. For more flexible control of the optimization outcomes, we propose to use a weighted cost function instead of the original Eq. (6)

$$\text{cost_function}(\{\bar{E}, \bar{\nu}, \bar{G}\}) = e^{-w_E(\bar{E}-\bar{E}_t)^2 - w_\nu(\bar{\nu}-\bar{\nu}_t)^2}, \quad (9)$$

where w_E and w_ν are two constants reflecting a bias on the optimization targets. We leave the explorations of a more adequately designed cost function as our future work.

Though we have already simplified the optimization problem to a relatively low dimensional parameter space, it is important to be aware that the problem is still highly non-convex. The searching path may finally lead to a local optimum.

4. Conclusions

We propose an optimization framework based on machine learning techniques to design composite mechanical metamate-

rials. We focus on controls of macroscopic elastic moduli and design optimal RVEs to achieve the goal. Results are verified by experimental measurements on multi-material 3D printed samples.

One limitation of this work is that the database of RVE samples are constructed via drawing samples from a artificially defined random process. Since we know precisely about the data generating process, it is possible to use more effective data compression methods than to use a VAE. For example, directly applying PCA to the database used in this work could have yielded a comparable performance to a nonlinear autoencoder model. However, the proposed scheme with VAEs are generally applicable to empirical databases whose structure may not be transparent. Promising future improvements on this work include adopting variants of VAEs like conditional variational autoencoder (CVAE) [41] for more regularized mappings from the latent space to the decoded samples, a more systematic way of choosing BayesOpt hyperparameters such as Gaussian process kernels and acquisition functions [37], etc. Finally, we wish to extend the work to 3D mechanical metamaterial designs.

Declaration of competing interest

The authors declare that they have no known competing financial interests or personal relationships that could have appeared to influence the work reported in this paper.

Acknowledgment

This work is partially supported by the Princeton Catalysis Initiative at Princeton University.

Appendix A. Computational homogenization

We use a homogenization method to compute the macroscopic material parameters. For an arbitrary RVE, we impose

Table 1
Comparisons between target values, optimization results and experiment outcomes.

True	\bar{E}_t (Target) 260 MPa	\bar{E}^* (Optimized) 505 MPa	\bar{E}_e (Exp) 562 MPa	$\bar{\nu}_t$ (Target) 0.400	$\bar{\nu}^*$ (Optimized) 0.404	$\bar{\nu}_e$ (Exp) 0.43
Normalized	\hat{E}_t (Target) 0.827	\hat{E}^* (Optimized) 0.898	\hat{E}_e (Exp) 0.910	$\hat{\nu}_t$ (Target) 1.70	$\hat{\nu}^*$ (Optimized) 1.74	$\hat{\nu}_e$ (Exp) 2.0

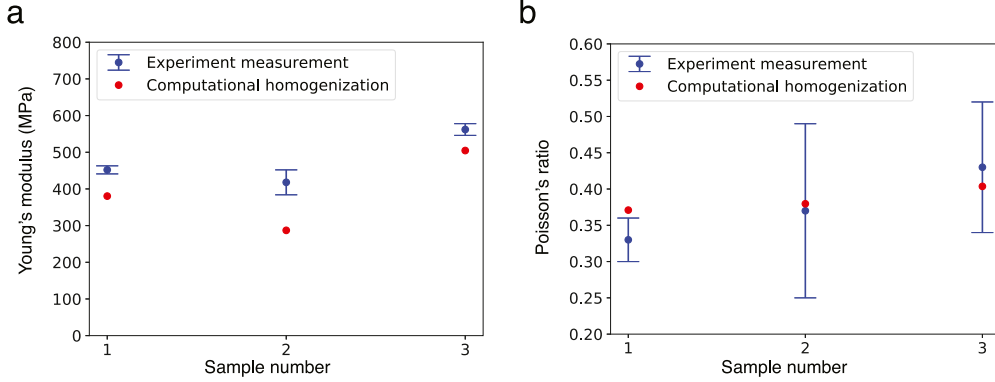


Fig. 6. Experimental validation. Left: macroscopic Young's modulus by experiment measurement and computational homogenization for the three RVEs in Fig. 4. Right: macroscopic Poisson's ratio by experiment measurement and computational homogenization for the same RVEs.

macroscopic deformations by prescribing the following periodic boundary conditions:

$$\mathbf{u}(\mathbf{x}) = \bar{\mathbf{h}} \cdot \mathbf{x} + \mathbf{u}^*(\mathbf{x}), \quad (\text{A.1})$$

where $\bar{\mathbf{h}} = \nabla \bar{\mathbf{u}}$ is the macroscopic displacement gradient and is uniform on the RVE. Essentially, Eq. (A.1) decomposes the total displacement of the RVE into a macroscopic (overall) part $\bar{\mathbf{u}} = \bar{\mathbf{h}} \cdot \mathbf{x}$ and a microscopic (fluctuating) part \mathbf{u}^* . Periodic boundary conditions are applied such that for RVE $ABCD$ in Fig. A.1, we have $\mathbf{u}_{AD}^* = \mathbf{u}_{BC}^*$ and $\mathbf{u}_{AB}^* = \mathbf{u}_{DC}^*$. A fine-mesh FEM calculation is used to solve for \mathbf{u} with such boundary conditions described above. Then the macroscopic strain energy density \bar{W} can be obtained via the average of W over the RVE:

$$\bar{W} = V^{-1} \int_V W dV, \quad (\text{A.2})$$

with V being the total volume of the RVE. Note that \bar{W} is also computed using Eq. (3). Therefore we are able to obtain an equation for the unknown macroscopic constitutive tensor $\bar{\mathbb{C}}$.

The choice of $\bar{\mathbf{h}}$ is not unique, though. In this work, since $\bar{\mathbb{C}}$ has three independent components, we pick three distinct $\bar{\mathbf{h}}$:

$$\begin{aligned} \bar{\mathbf{h}}_1 &= \epsilon \mathbf{e}_1 \otimes \mathbf{e}_1, \\ \bar{\mathbf{h}}_2 &= \epsilon \mathbf{e}_2 \otimes \mathbf{e}_2, \\ \bar{\mathbf{h}}_3 &= \frac{\epsilon}{2} (\mathbf{e}_1 \otimes \mathbf{e}_2 + \mathbf{e}_2 \otimes \mathbf{e}_1), \end{aligned} \quad (\text{A.3})$$

where ϵ is a small constant. The resulting three independent equations are used to solve for $\bar{\mathbb{C}}$, thus completing the homogenization procedures for such a RVE.

Appendix B. Formulation of a VAE

We present a more detailed description of the formulation of a VAE, particularly the one used in this work. As a generative model, a VAE aims at simulating the underlying data generating process. The observable RVE image data are assumed to be generated from a high dimensional probability distribution $p(\mathbf{x})$ where $\mathbf{x} \in \mathbb{R}^{28 \times 28}$. Approximating $p(\mathbf{x})$ with a parametrized distribution $p_\theta(\mathbf{x})$ directly is considered not feasible [42]. To see this,

the maximum likelihood estimate given dataset $\{\mathbf{x}^{(i)}\}$ yields

$$\max_{\theta} \sum_i \ln p_\theta(\mathbf{x}^{(i)}) = \max_{\theta} \sum_i \ln \left(\int_z p_\theta(\mathbf{x}^{(i)}, z) dz \right), \quad (\text{B.1})$$

where marginalization over the latent variable z is often intractable. Note that z typically lives in a low dimensional space. In our work, $z \in \mathbb{R}^{10}$ serves as the design parameter. Based on the variational principle, an auxiliary function variable $q \in \mathcal{Q}$ (\mathcal{Q} is the variational family) is introduced to reformulate Eq. (B.1) as:

$$\begin{aligned} \max_{\theta} \sum_i \left(\ln p_\theta(\mathbf{x}^{(i)}) - \min_{q \in \mathcal{Q}} \mathbb{KL}(q(z) \parallel p_\theta(z | \mathbf{x}^{(i)})) \right) \\ = \max_{\theta} \sum_i \max_{q \in \mathcal{Q}} \mathbb{E}_{q(z)} \left[\ln \frac{p_\theta(\mathbf{x}^{(i)}, z)}{q(z)} \right], \end{aligned} \quad (\text{B.2})$$

where $\mathbb{KL}(\cdot \parallel \cdot)$ is the Kullback–Leibler divergence [43]. The optimization problem is still rather complicated, though, since it is a bi-level optimization problem and involves a function variable q .

To overcome these difficulties, VAEs adopt an approximate approach. By amortizing the computational cost, VAEs propose to solve the following optimization problem:

$$\max_{\theta, \phi} \sum_i \mathbb{E}_{q_\phi(z | \mathbf{x}^{(i)})} \left[\ln \frac{p(z) p_\theta(\mathbf{x}^{(i)} | z)}{q_\phi(z | \mathbf{x}^{(i)})} \right], \quad (\text{B.3})$$

where $q_\phi(z | \mathbf{x}^{(i)})$ is a neural network function parametrized by ϕ (known as the encoder function), and $p_\theta(\mathbf{x}^{(i)} | z)$ is another neural network function parametrized by θ (known as the decoder function). Eq. (B.3) is the loss function of a VAE and can be rewritten into a more familiar format:

$$\min_{\theta, \phi} \sum_i \left(-\mathbb{E}_{q_\phi(z | \mathbf{x}^{(i)})} \left[\ln p_\theta(\mathbf{x}^{(i)} | z) \right] + \mathbb{KL}(q_\phi(z | \mathbf{x}^{(i)}) \parallel p(z)) \right). \quad (\text{B.4})$$

In Eq. (B.4), the first term is the reconstruction loss of the i th data point $\mathbf{x}^{(i)}$ while the second term is the KL-divergence between two multivariate Gaussian distributions.

We randomly split our database (containing 3000 data points) into a training set (80% of the data) and a test set (the rest 20%). We use mini-batch stochastic gradient descent with Adam optimizer [44] to train the VAE with the loss function defined by

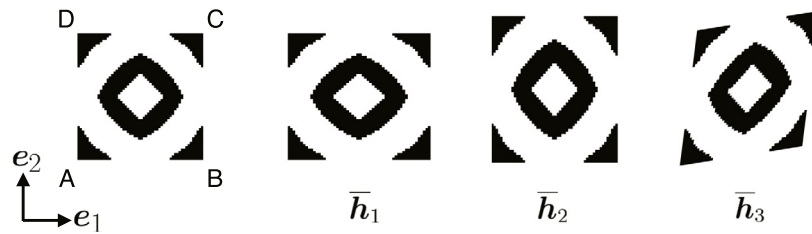


Fig. A.1. A sample RVE in its reference configuration (leftmost), and illustration of the deformed configurations with imposed macroscopic displacement gradient conditions (right three).

Eq. (B.4). Learning rate is set to be 10^{-3} while batch size is set to be 64. The training time is typically within 1 min on a personal computer to achieve a satisfactory model performance.

References

- [1] X. Zheng, H. Lee, T.H. Weisgraber, M. Shusteff, J. DeOtte, E.B. Duoss, J.D. Kuntz, M.M. Biener, Q. Ge, J.A. Jackson, et al., Ultralight, ultrastiff mechanical metamaterials, *Science* 344 (6190) (2014) 1373–1377.
- [2] M. Kadic, T. Bückmann, N. Stenger, M. Thiel, M. Wegener, On the practicality of pentamode mechanical metamaterials, *Appl. Phys. Lett.* 100 (19) (2012) 191901.
- [3] K. Bertoldi, P.M. Reis, S. Willshaw, T. Mullin, Negative Poisson's ratio behavior induced by an elastic instability, *Adv. Mater.* 22 (3) (2010) 361–366.
- [4] S. Yuan, C.K. Chua, K. Zhou, 3D-printed mechanical metamaterials with high energy absorption, *Adv. Mater. Technol.* 4 (3) (2019) 1800419.
- [5] D. Chen, X. Zheng, Multi-material additive manufacturing of metamaterials with giant, tailorable negative Poisson's ratios, *Sci. Rep.* 8 (1) (2018) 9139.
- [6] X. Ren, J. Shen, P. Tran, T.D. Ngo, Y.M. Xie, Design and characterisation of a tuneable 3D buckling-induced auxetic metamaterial, *Mater. Des.* 139 (2018) 336–342.
- [7] P. Sitthi-Amorn, J.E. Ramos, Y. Wang, J. Kwan, J. Lan, W. Wang, W. Matusik, MultiFab: a machine vision assisted platform for multi-material 3D printing, *ACM Trans. Graph.* 34 (4) (2015) 1–11.
- [8] P. Vogiatzis, S. Chen, X. Wang, T. Li, L. Wang, Topology optimization of multi-material negative Poisson's ratio metamaterials using a reconciled level set method, *Comput. Aided Des.* 83 (2017) 15–32.
- [9] M. Mirzaali, A. Caracciolo, H. Pahlavani, S. Janbaz, L. Vergani, A. Zadpoor, Multi-material 3D printed mechanical metamaterials: Rational design of elastic properties through spatial distribution of hard and soft phases, *Appl. Phys. Lett.* 113 (24) (2018) 241903.
- [10] M. Mirzaali, R. Hedayati, P. Vena, L. Vergani, M. Strano, A. Zadpoor, Rational design of soft mechanical metamaterials: Independent tailoring of elastic properties with randomness, *Appl. Phys. Lett.* 111 (5) (2017) 051903.
- [11] B. Zhu, M. Skouras, D. Chen, W. Matusik, Two-scale topology optimization with microstructures, *ACM Trans. Graph.* 36 (4) (2017) 1.
- [12] C. Schumacher, B. Bickel, J. Rys, S. Marschner, C. Daraio, M. Gross, Microstructures to control elasticity in 3D printing, *ACM Trans. Graph.* 34 (4) (2015) 1–13.
- [13] T. Xue, A. Beatson, S. Adriaenssens, R.P. Adams, Amortized finite element analysis for fast PDE-constrained optimization, in: *ICLR 2020 Workshop on Integration of Deep Neural Models and Differential Equations*, 2020.
- [14] A. Beatson, J.T. Ash, G. Roeder, T. Xie, R.P. Adams, Learning composable energy surrogates for PDE order reduction, 2020, arXiv preprint [arXiv:2005.06549](https://arxiv.org/abs/2005.06549).
- [15] T. Xue, A. Beatson, M. Chiaramonte, G. Roeder, J.T. Ash, Y. Menguc, S. Adriaenssens, R.P. Adams, S. Mao, A data-driven computational scheme for the nonlinear mechanical properties of cellular mechanical metamaterials under large deformation, *Soft Matter* (2020).
- [16] D.P. Kingma, M. Welling, Auto-encoding variational bayes, 2013, arXiv preprint [arXiv:1312.6114](https://arxiv.org/abs/1312.6114).
- [17] I. Goodfellow, J. Pouget-Abadie, M. Mirza, B. Xu, D. Warde-Farley, S. Ozair, A. Courville, Y. Bengio, Generative adversarial nets, in: *Advances in Neural Information Processing Systems*, 2014, pp. 2672–2680.
- [18] J. Moćkus, On Bayesian methods for seeking the extremum, in: *Optimization Techniques IFIP Technical Conference*, Springer, 1975, pp. 400–404.
- [19] R. Gómez-Bombarelli, J.N. Wei, D. Duvenaud, J.M. Hernández-Lobato, B. Sánchez-Lengeling, D. Sheberla, J. Aguilera-Iparraguirre, T.D. Hirzel, R.P. Adams, A. Aspuru-Guzik, Automatic chemical design using a data-driven continuous representation of molecules, *ACS Cent. Sci.* 4 (2) (2018) 268–276.
- [20] S. Eismann, S. Bartzsch, S. Ermon, Shape optimization in laminar flow with a label-guided variational autoencoder, 2017, arXiv preprint [arXiv:1712.03599](https://arxiv.org/abs/1712.03599).
- [21] Z. Yang, X. Li, L. Catherine Brinson, A.N. Choudhary, W. Chen, A. Agrawal, Microstructural materials design via deep adversarial learning methodology, *J. Mech. Des.* 140 (11) (2018).
- [22] T. Guo, D.J. Lohan, R. Cang, M.Y. Ren, J.T. Allison, An indirect design representation for topology optimization using variational autoencoder and style transfer, in: *2018 AIAA/ASCE/AHS/ASC Structures, Structural Dynamics, and Materials Conference*, 2018, p. 0804.
- [23] Z. Hashin, S. Shtrikman, A variational approach to the theory of the elastic behaviour of multiphase materials, *J. Mech. Phys. Solids* 11 (2) (1963) 127–140.
- [24] B. Budiansky, On the elastic moduli of some heterogeneous materials, *J. Mech. Phys. Solids* 13 (4) (1965) 223–227.
- [25] R. Hill, A self-consistent mechanics of composite materials, *J. Mech. Phys. Solids* 13 (4) (1965) 213–222.
- [26] J. Willis, Bounds and self-consistent estimates for the overall properties of anisotropic composites, *J. Mech. Phys. Solids* 25 (3) (1977) 185–202.
- [27] L. Kharevych, P. Mullen, H. Owghadi, M. Desbrun, Numerical coarsening of inhomogeneous elastic materials, *ACM Trans. Graph.* 28 (3) (2009) 1–8.
- [28] T. Wallin, J. Pikul, S. Bodkhe, B. Peele, B. Mac Murray, D. Theriault, B. McEnerney, R. Dillon, E. Giannelis, R. Shepherd, Click chemistry stereolithography for soft robots that self-heal, *J. Mater. Chem. B* 5 (31) (2017) 6249–6255.
- [29] J.N. Reddy, *An Introduction to Continuum Mechanics*, Cambridge University Press, 2007.
- [30] M.E. Gurtin, *An Introduction to Continuum Mechanics*, Academic Press, 1982.
- [31] M. Alnæs, J. Blechta, J. Hake, A. Johansson, B. Kehlet, A. Logg, C. Richardson, J. Ring, M.E. Rognes, G.N. Wells, The FEniCS project version 1.5, *Arch. Numer. Softw.* 3 (100) (2015).
- [32] C.M. Bishop, *Pattern Recognition and Machine Learning*, Springer, 2006.
- [33] A. Paszke, S. Gross, S. Chintala, G. Chanan, E. Yang, Z. DeVito, Z. Lin, A. Desmaison, L. Antiga, A. Lerer, Automatic differentiation in pytorch, 2017.
- [34] J.D. Hyman, C. Winter, Stochastic generation of explicit pore structures by thresholding Gaussian random fields, *J. Comput. Phys.* 277 (2014) 16–31.
- [35] Z. Jiang, W. Chen, C. Burkhart, Efficient 3D porous microstructure reconstruction via Gaussian random field and hybrid optimization, *J. Microsc.* 252 (2) (2013) 135–148.
- [36] I.T. Jolliffe, Principal components in regression analysis, in: *Principal Component Analysis*, Springer, 1986, pp. 129–155.
- [37] B. Shahriari, K. Swersky, Z. Wang, R.P. Adams, N. De Freitas, Taking the human out of the loop: A review of Bayesian optimization, *Proc. IEEE* 104 (1) (2015) 148–175.
- [38] D. Driess, P. Englert, M. Toussaint, Constrained bayesian optimization of combined interaction force/task space controllers for manipulations, in: *2017 IEEE International Conference on Robotics and Automation (ICRA)*, IEEE, 2017, pp. 902–907.
- [39] E. Bakshy, L. Dworkin, B. Karrer, K. Kashin, B. Letham, A. Murthy, S. Singh, AE: A Domain-Agnostic Platform for Adaptive Experimentation, *SemanticScholar*, 2018.
- [40] T.J. Wallin, L. Simonsen, W. Pan, K. Wang, E. Giannelis, R.F. Shepherd, Y. Menguc, 3D printable tough silicone double networks, *Nature Commun.* (2020).
- [41] K. Sohn, H. Lee, X. Yan, Learning structured output representation using deep conditional generative models, in: *Advances in Neural Information Processing Systems*, 2015, pp. 3483–3491.
- [42] C. Doersch, Tutorial on variational autoencoders, 2016, arXiv preprint [arXiv:1606.05908](https://arxiv.org/abs/1606.05908).
- [43] S. Kullback, R.A. Leibler, On information and sufficiency, *Ann. Math. Stat.* 22 (1) (1951) 79–86.
- [44] D.P. Kingma, J. Ba, Adam: A method for stochastic optimization, 2014, [arxiv:1412.6980](https://arxiv.org/abs/1412.6980).